Neutron scattering study of the charge-density wave transitions in $2H$-$TaSe_2$ and $2H$-$NbSe_2$

D. E. Moncton*†
Physics Department, Massachusetts Institute of Technology, Cambridge, Massachusetts 02139 and Brookhaven National Laboratory, Upton, New York 11973

J. D. Axe*
Brookhaven National Laboratory, Upton, New York 11973

F. J. DiSalvo
Bell Laboratories, Murray Hill, New Jersey 07974

(Received 20 December 1976)

We have used the triple-axis neutron-scattering technique to study $2H$-$TaSe_2$ and $2H$-$NbSe_2$ which undergo charge-density wave transitions at $T_0 = 122.3$ K and $T_0 = 33.5$ K, respectively. The transitions in both compounds appear to be second-order and involve atomic displacements of Σ_1 symmetry. At inception, the superlattices in both compounds have nearly identical incommensurate wave vectors with magnitude $q_\delta = 1/3(1-\delta)a^*$, with $\delta \sim 0.02$. The $NbSe_2$ superlattice remains incommensurate to 5 K but $TaSe_2$ undergoes a first-order lock-in transition where $\delta \to 0$ at 90 K. The temperature dependence of the superlattice wave vector $\vec{q}$ in the incommensurate phase and the lock-in transition are discussed using a free energy involving third-order "umklapp" terms and a secondary order parameter. The secondary lattice distortion which is predicted in this model is observed experimentally. Most phonon branches having energies less than 10 meV with propagation vectors in the $[\zeta 00]$ and $[00\zeta]$ directions have been measured at 300 K. Strong anomalies are found in the $\Sigma_1[\zeta 00]$ phonon branches in both materials near the wave vector $\vec{q}_c = (1/3, 0, 0)$ characteristic of the low-temperature superlattices. Substantial softening of this phonon is observed as the transition is approached. In addition, the spectral profile exhibits a central peak which is not measurably inelastic.

I. INTRODUCTION

The intriguing properties of the transition-metal dichalcogenides have been the subject of increasingly active study. To a large extent current interest has been promoted by the discovery that many of the metallic layered compounds exhibit charge-density wave (CDW) instabilities.[1-3] The CDW transition occurs when a static electronic charge-density wave of wave vector $\vec{q}$ develops within the conduction-electron gas and a gap opens at the Fermi surface. The occurrence of such an electronic instability is thought to require a large electronic susceptibility $\chi_0(\vec{q})$ which may develop as a result of the nesting of various pieces of Fermi surface. Although suggested details[2,4] of these nesting features have yet to be confirmed, they are undoubtedly a result of the anisotropy characteristic of the layered, two-dimensional structures of these materials. The structure of the $2H$ polytype is shown in Fig. 1 with the crystallographic data for $TaSe_2$ and $NbSe_2$.

Since the wave vector of the CDW is determined by the Fermi surface, it will not in general be commensurate with the lattice. The complex quantity which represents the CDW amplitude and phase may be taken as the order parameter for the transition. The crystal lattice is fundamentally involved in the transformation, since the large Coulomb energy of the CDW must be reduced by the accommodating motion of the ions. As a result of the linear coupling between the lattice and the charge density, the lattice distortion which develops is also proportional to the order parameter. Therefore, the CDW transition is properly a displacive transition and one expects phonon softening to be evident.[5]

A variety of experiments to date have confirmed that CDW behavior occurs in many of the metallic layered dichalcogenides. Specifically electron-diffraction experiments by Wilson *et al.*[2] on $1T$-$TaSe_2$ have documented the development of an incommen-

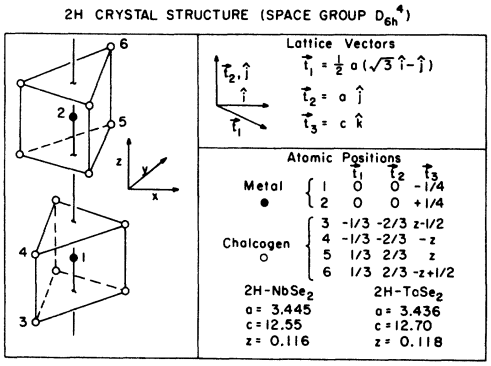

FIG. 1. $2H$ structure and crystallographic parameters for $2H$-$TaSe_2$ and $2H$-$NbSe_2$.

surate superlattice below $T_0 \approx 600$ K and showed by doping the compounds with Ti that the magnitude of the CDW wave vector depends explicitly on a Fermi-surface dimension. Subsequently, neutron-scattering experiments[3] by the present authors demonstrated the formation of incommensurate superlattices in both $2H$-$NbSe_2$ ($T_0 = 33.5$ K) and $2H$-$TaSe_2$ ($T_0 = 122.3$ K) and the presence of precursor phonon softening at the superlattice wave vector. A particularly interesting discovery in both of the above diffraction studies was the existence of a second phase transition which occurs below T_0 in both $1T$-$TaSe_2$ and $2H$-$TaSe_2$ when the incommensurate superlattices adopt commensurate structures. We have found that it is possible to account qualitatively for the temperature-dependent incommensurability, as well as the transition to the commensurate structure, by using a simple Landau order-parameter theory. It is the purpose of this article to give a full account of these experiments and their interpretation. In Sec. II we will describe the experimental details including spectrometer configurations and sample preparation. The results of elastic-neutron-diffraction studies are described in Sec. III, and the inelastic-scattering results are discussed in Sec. IV. Finally in Sec. V we will outline a Landau theory and compare it with the data.

II. EXPERIMENTAL PROCEDURES

A. Spectrometer configurations

The present experiments were performed on triple-axis spectrometers at the Brookhaven National Laboratory High-Flux Beam Reactor. All data were taken using oriented pyrolytic graphite crystals to monochromate, analyze, and filter the beam. A number of spectrometer configurations were used:

(i) Double-axis configuration for integrated intensity measurements. No analyzer was used and typical collimation was 20′-20′-open-open (sequentially from beam port collimator).

(ii) Triple-axis elastic configuration for high-$\vec{Q}$ resolution. An analyzer set for elastic scattering was used to remove inelastic background and improve resolution. Collimation was $(20')^4$ or $(10'-20')^2$ in most cases.

(iii) Conventional triple-axis inelastic configuration for measurement of phonon dispersion relations. Collimation was either $(40')^4$ or $20'-(40')^3$.

Configurations (i) and (ii) employed an incident beam of energy between 13.0 and 14.8 meV. When necessary, filtering was done with 4 in. of tuned pyrolytic graphite. No significant amount of $\frac{1}{2}\lambda$ or $\frac{1}{3}\lambda$ contamination could be detected. Configuration (iii) used a variety of incident beam energies in the range 13.0–45.0 meV. Filtering was done when necessary (or possible). The scans were either of constant-$\vec{Q}$ or constant-E type. In the constant-$\vec{Q}$ method it is possible to change either $\vec{k}_i$ or $\vec{k}_f$. When scanning $\vec{k}_i$, $\vec{k}_f$ was fixed at 13.5 meV, and filtering was done after the sample.

B. Sample preparation

Crystals were grown specifically for this study at both Bell Laboratories and Brookhaven Laboratory. In both cases the original starting metals (Nb, Ta) were of 99.95% purity and Se was 99.9995% pure. Stoichiometric amounts of the elements were placed in small evacuated (<10 μm) quartz tubes and reacted at about 900 °C for several days. Polycrystalline powder charges obtained in this way were placed in a square quartz tube ($1.6 \times 1.6 \times 20.0$ cm^3) with iodine vapor (5 mg/cm^3 of tube volume). This amount of iodine produces a vapor pressure of about 3 atm at 700 °C. It has been found that crystals of both $2H$-$NbSe_2$ and $2H$-$TaSe_2$ grow with repeatable stoichiometry when the vapor is slightly rich in chalcogen. Therefore, the powder charge is supplemented with 0.3 mg/cm^3 excess Se for the growth of $2H$-$TaSe_2$ and 1 mg/cm^3 for $2H$-$NbSe_2$. Vapor transport growth at Bell Laboratories was carried out in tube furnaces with adjustable temperature gradients. The growth zone was kept at 700 °C (750 °C) for $2H$-$TaSe_2$ ($2H$-$NbSe_2$), while the powder charge temperature was elevated by about 50 °C. Since the $2H$ polytype is stable at room temperature, no quenching procedure was needed. Crystals of $2H$-$TaSe_2$ typically of mass 50 mg were produced with the largest being 150 mg. Only one usable crystal of $2H$-$NbSe_2$ of mass 10 mg was obtained.

The best crystal of $2H$-$TaSe_2$ was grown at Brookhaven in a furnace which was equipped with a programmable heater. With the growth zone at 700 °C the charge zone was maintained at 650 °C for 2 d. Such a reverse gradient condition transports away any material which may have been accidentally in the growth zone. Then over a period of 5–7 d the charge zone temperature was raised to 750 °C where it remained for four weeks. This method yielded a number of crystals in the 100-mg range and one of 600 mg. In summary, we used the 150- and 600-mg crystals of $2H$-$TaSe_2$, the 10-mg crystal of $2H$-$NbSe_2$ and, in addition, a $2H$-$NbSe_2$ crystal lent to us by Frindt.[6]

The two crystals of $2H$-$TaSe_2$ showed essentially identical behavior of their CDW transitions. Both had onset temperatures of $T_0 = 122.3 \pm 0.1$ K, and similar values of δ and lock-in temperature (see Sec. III for an explanation of these quantities). The 600-mg $TaSe_2$ crystal had a mosaic spread of about

0.5 deg full width at half maximum (FWHM) as obtained in a diffraction rocking curve; the 150-mg crystal had a slightly better mosaic spread. The Frindt $NbSe_2$ crystal did not develop an $\frac{1}{3}a^*$ superlattice, and was used only to obtain 300-K phonon data. The 10-mg $NbSe_2$ sample was the only available crystal suitable for neutron studies of the CDW transition. Huntley and Frindt,[7] in a study of the transport properties of $2H$-$NbSe_2$, showed that better crystals have higher CDW transition temperatures. The 10-mg crystal transformed at 33.5 K, which is as high as any value reported in the literature. For this reason, and because of the similarity to the $2H$-$TaSe_2$ results, we feel the $2H$-$NbSe_2$ data also represent the pure material.

III. ELASTIC-SCATTERING RESULTS

A. Incommensurate phases and the lock-in transition

Our study of the temperature dependence of the Bragg intensities shows that superlattice formation occurs in an apparently second-order manner in both $NbSe_2$ ($T_0 = 33.5$ K) and $TaSe_2$ ($T_0 = 122.3$ K). Furthermore we find that the wave vector characterizing the superlattice is also temperature dependent. Figure 2 shows the results of high-resolution scans along $[\zeta 00]$ at various temperatures below T_0 in $TaSe_2$. These data were taken using the triple-axis spectrometer geometry [configuration (ii), Sec. IIA]. Collimation was tightened as the temperature was lowered. $\frac{1}{3}\lambda$ contamination was removed from the incident beam by a 4-in. stack of tuned pyrolytic graphite filters. These data provide clear evidence of three novel features in the development of the superlattice:

(i) The wave vector characterizing the superlattice just below T_0 is *not* exactly commensurate, $\vec{q}_c = (\frac{1}{3}, 0, 0)$, but is rather $\vec{q}_\delta = (1-\delta)\vec{q}_c$, with $\delta \simeq 0.02$

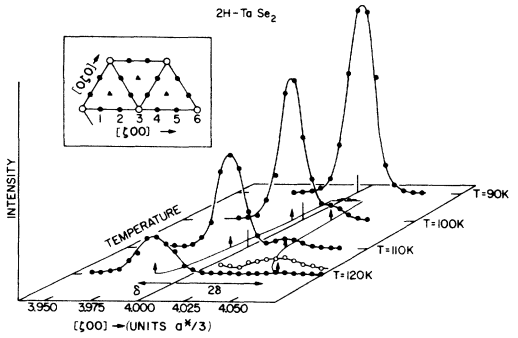

FIG. 2. Elastic scans along $[\zeta 00]$ showing the incommensurate primary peak at $\zeta = \frac{1}{3}(4-\delta)$ and a secondary peak at $\zeta = \frac{1}{3}(4+2\delta)$. Open circles indicate multiplication by 10. In the inset the filled circles are the $\frac{1}{3}a^*$ reciprocal superlattice and the open circles are the main Bragg peaks of the $2H$ structure.

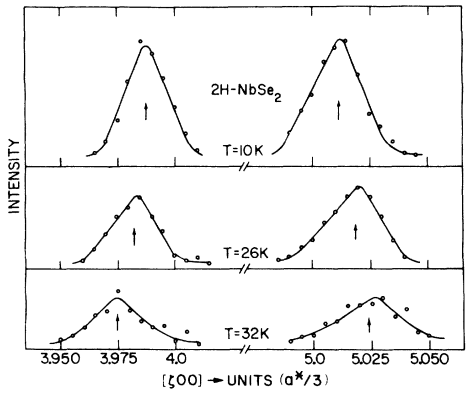

FIG. 3. Elastic scans along $[\zeta 00]$ showing incommensurate peaks $\zeta = \frac{1}{3}(4-\delta)$ and $\zeta = \frac{1}{3}(5+\delta)$.

and temperature dependent.

(ii) There exists an apparently first-order phase transition[8] near 90 K in which $\delta \to 0$, and the superlattice remains commensurate below this temperature.

(iii) In the incommensurate regime the primary lattice distortion of wave vector $\vec{q}_\delta$ is accompanied by a weaker secondary lattice distortion of wave vector $\vec{q}_{2\delta} = (1+2\delta)\vec{q}_c$. Bragg scattering at wave vector $\vec{q}_{2\delta}$ can develop simply as a diffraction harmonic from a lattice distortion having only a $\vec{q}_\delta$ component. However, estimates indicate this effect to be below 10^{-4} times the intensity of the neighboring $\vec{q}_\delta$ peak. Therefore, the intensity observed at $\vec{q}_{2\delta}$ requires an actual lattice distortion having wave vector $\vec{q}_{2\delta}$. Our search for this scattering was motivated by free-energy considerations to be discussed in Sec. V. There we will show that the secondary distortion plays a vital role in the temperature dependence of δ.

In $NbSe_2$ a similarly incommensurate superlattice is observed below T_0 (Fig. 3), yet no lock-in transition occurs above 5 K. The sample was too small to observe a $\vec{q}_{2\delta}$ peak. The temperature dependence of δ and (for $TaSe_2$) the intensity ratio $I_{2\delta}/I_\delta$ have been extracted from a larger set of curves similar to those in Figs. 2 and 3 by fitting Gaussian-plus-background functions with a least-squares technique. These data are compiled in Fig. 4(a) and 4(c), respectively. Model calculations based on the free-energy functions described in Sec. V are shown in Figs. 4(b) and 4(d).

We have measured the temperature dependence of the integrated intensity of many primary peaks in $NbSe_2$ and $TaSe_2$, and all have a temperature dependence similar to that shown in Fig. 5. The data were obtained in θ-2θ scans using the spectrometer in configuration (i). For $TaSe_2$ in the incommensurate regime the intensities have been corrected for the fact that the scans include the $\vec{q}_{2\delta}$ peak.

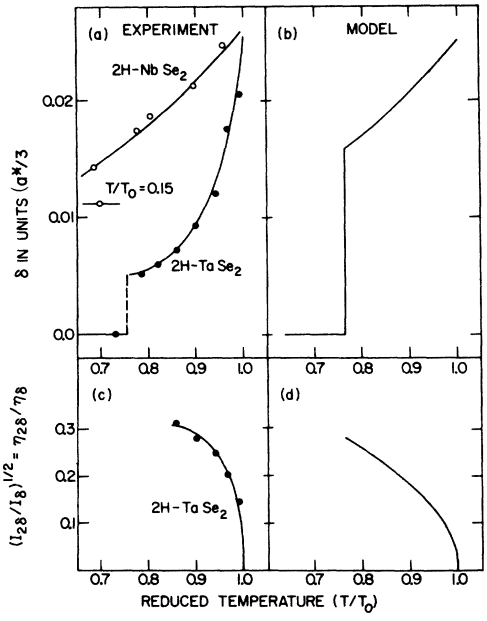

FIG. 4. Temperature dependence of δ and $\eta_{2\delta}/\eta_{\delta}$ as measured [(a) and (c)] as as predicted [(b) and (d)] by the model described in Sec. V.

Such a secondary peak is not observable in $NbSe_2$; therefore, no such correction has been made. The transition at T_0 appears continuous in both cases; however, it is impossible to rule out the presence of a small first-order discontinuity. For example, the first-order nature of the spin density wave transition[9] in Cr, as well as the displacive transition[10] in Nb_3Sn, are difficult to observe experimentally.

B. Atomic displacements in the CDW state

To determine the atomic displacements in the CDW state, we have studied the commensurate phase of $TaSe_2$. We feel that the atomic displacements which result from the present analysis characterize the commensurate and the incommensurate phase of $TaSe_2$ as well as the incommensurate phase of $NbSe_2$. We draw this conclusion because the distribution of intensity among the various superlattice peaks appears generally the same in $TaSe_2$ above and below the lock-in transition as it does in $NbSe_2$. The commensurate $\frac{1}{3}a^*$ superlattice shown schematically in Fig. 6 is found in $TaSe_2$ below 90 K. The solid circles are called "primary" points of the superlattice, since diffracted intensity associated with them is generated by scattering processes characterized by a single wave vector from the set $\{\pm\vec{q}_1, \pm\vec{q}_2, \pm\vec{q}_3\}$. Scattering associated with the crosses involves at least two different wave vectors.

We have measured 26 primary superlattice peaks

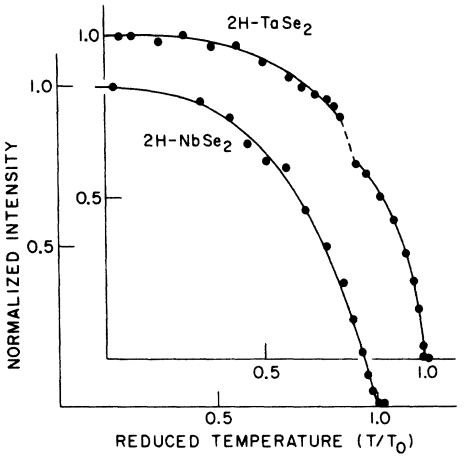

FIG. 5. Temperature dependence of the $((5+\delta)/3, 0, 0)$ superlattice peaks in $TaSe_2$ and $NbSe_2$. The break in the $TaSe_2$ curve marks the lock-in transition.

in the $[hk0]$ or $[h0l]$ zones. ϕ scans were taken using the double-axis geometry [configuration (i)] at a sample temperature of 5 K. Background intensities measured just above T_0 were subtracted in all cases. Debye-Waller corrections for thermal motion of the atoms are normally negligible[11] at 5 K. However, it was important to correct for neutron absorption since the Ta-capture cross section is quite large. The flatplate growth habit of these crystals allowed data taken in the $[h0l]$ zone

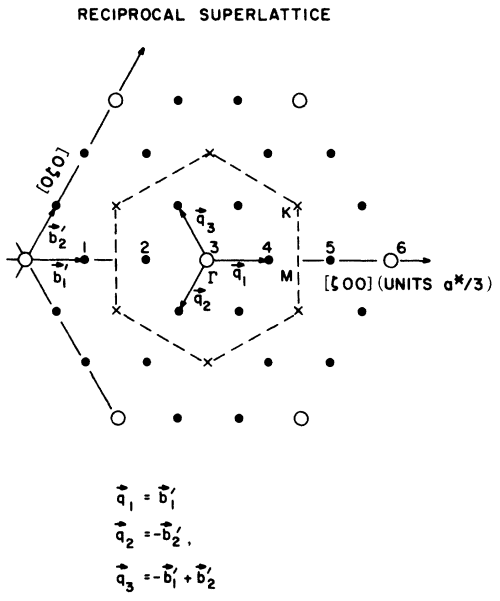

FIG. 6. $\frac{1}{3}a^*$ reciprocal superlattice. The open circles are the Bragg points of the $2H$ structure. The wave vectors $\vec{q}_1$, $\vec{q}_2$, $\vec{q}_3$ which characterize the lattice distortion are shown.

to be easily corrected, while in the $[hk0]$ zone corrections were not possible. Therefore, the error associated with the $[hk0]$ data is somewhat larger.

Multiple scattering effects can significantly alter the intensities of the weaker superlattice reflections. We have taken the following precautions to avoid these effects: (i) A long neutron wavelength (2.5 Å) was used to minimize the number of possible multiple processes. (ii) Most superlattice intensities were checked at several wavelengths near 2.5 Å. Peaks having strong intensity variations were discarded.

To determine the magnitudes of the atomic shifts, it is necessary to know the absolute intensities of the superlattice reflections. We attempted to use the Bragg peaks of the $2H$ structure as a calibration for these measurements. Their structure factors are known, and their intensities are essentially unaffected by the CDW transition. However, the measured intensity ratio of the strong (008) $2H$ peak to the weak (100) peak (indices of the $2H$ reciprocal lattice) was considerably smaller than the calculated value. This discrepancy is probably caused by (i) a decrease in the (008) peak intensity as a result of extinction; and/or (ii) an increase in the (100) peak intensity by multiple scattering. In support of (ii) we have observed variations by over a factor of 2 in the intensity of the (100) peak as the incident wavelength is changed. As a result of these problems, it has not been possible to normalize the superlattice intensity data unambiguously. This uncertainty in the absolute intensity scale ultimately results in an uncertainty in the scale of the atomic displacement magnitudes, but does not affect phases or relative magnitudes.

Experimentally, the observed scattering has hexagonal symmetry, and occurs in (hkl) planes with $l=0,1,\ldots,n$. The superlattice reflections are indexed in terms of new reciprocal-lattice vectors $\vec{b}_1'=\frac{1}{3}\vec{b}_1$, $\vec{b}_2'=\frac{1}{3}\vec{b}_2$, and $\vec{b}_3'=\vec{b}_3$, where the vectors $\vec{b}_1$, $\vec{b}_2$, and $\vec{b}_3$ are the reciprocal-lattice vectors of the $2H$ structure. Hexagonal symmetry of the superlattice does not imply that three plane-waves (a "triple-$\vec{q}$" state) coexist microscopically in the crystal since an equal distribution of three "single-$\vec{q}$" domains would produce the same pattern. However, the existence of scattering at the superlattice points denoted by crosses in Fig. 6 requires that displacement waves with different wave vectors coexist in coherent regions of the crystal. We take this as evidence that a multiple-$\vec{q}$ ground state occurs. Since we will show in Sec. V that a two-$\vec{q}$ state is not energetically favorable, a triple-$\vec{q}$ state is most likely the correct description. Indeed electron diffraction experiments[2] have failed to reveal single-$\vec{q}$ domains with aperture sizes as small as one micron.

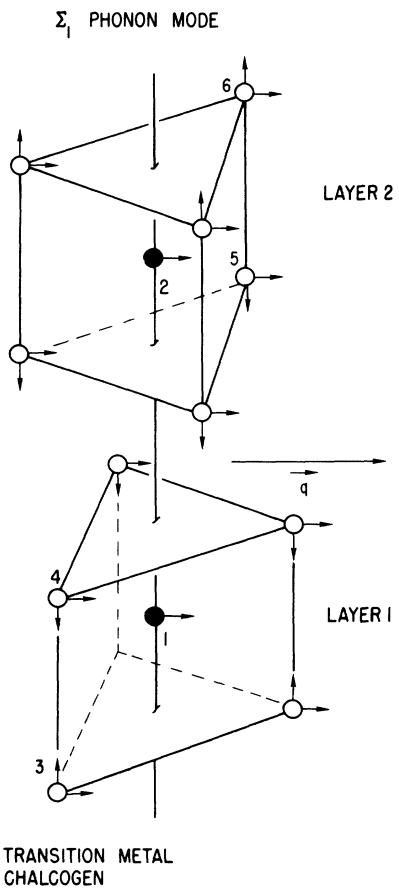

FIG. 7. Atomic displacements characteristic of Σ_1 symmetry.

The superlattice intensities are maximized in a pattern which indicates that the atomic displacements are predominantly longitudinal and have Σ_1 symmetry, as shown in Fig. 7. Assuming that an eigenvector $\vec{e}_\kappa$ transforming as a single representation will describe the low-temperature phase, symmetry constraints reduce the number of independent atomic displacement parameters considerably, as discussed in the Appendix. For displacements of Σ_1 symmetry there are six independent parameters which represent the magnitudes and phases, respectively, of the Ta-atom motion in the $\hat{x}$ direction $(\epsilon_{1x}^1, \phi_{1x}^1)$ and the Se-atom motion in the $\hat{x}$ direction $(\epsilon_{3x}^1, \phi_{3x}^1)$ and in the $\hat{z}$ direction $(\epsilon_{3z}^1, \phi_{3z}^1)$. To extract the parameters from the structure factor data, a linearized least-squares procedure was used. Structure factor and derivative expressions were developed analytically using the atomic displacements given by

$$\vec{u}_{l\kappa}=\sum_{\vec{q}} \tfrac{1}{2}\left[\vec{e}_\kappa(\vec{q})e^{i\vec{q}\cdot\vec{R}_l}+\vec{e}_\kappa^{\,*}(\vec{q})e^{-i\vec{q}\cdot\vec{R}_l}\right] \qquad (3.1)$$

for the κth atom in the lth unit cell. Here the sum

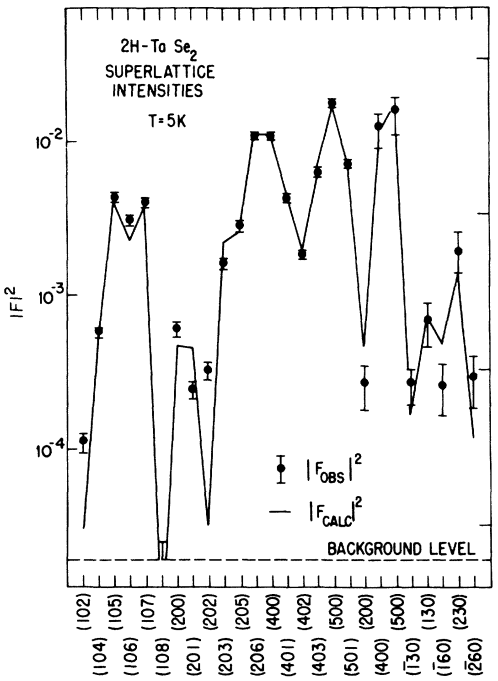

FIG. 8. Comparison of observed and calculated superlattice structure factors (F^2). The calculated structure factors are based on a model of atomic displacement of Σ_1 symmetry. Indices are those of the $\frac{1}{3}a^*$ superlattice.

may contain contributions from each of the three symmetry-equivalent wave vectors $\vec{q}_1$, $\vec{q}_2$, and $\vec{q}_3$. Using an eigenvector $\vec{e}_\kappa(\vec{q})$ having Σ_1 symmetry, and assuming a triple-$\vec{q}$ state, the optimum fit to the structure factor data is given in Fig. 8 and the resulting displacement parameters are given in Table I. The displacement magnitudes given in Table I are lower limit values. The aforementioned difficulties in intensity calibration result in upper limit values that are a factor of 1.9 larger than those given in the table. The magnitudes scale simply by an overall constant as a result of the approximate linear dependence of the structure factor on displacement, for small displacements.

The in-layer displacement of the Ta atoms (ϵ^1_{1x}) is larger than and in opposition to the Se in-layer displacement (ϵ^1_{3x}). We find a significant phase shift $2\phi^1_{1x} = 1.6$ rad between Ta motion in the two layers. This shift may arise because Coulomb forces cause the CDW maxima in one layer to avoid those in the adjacent layer. The fit is insensitive to a change in the overall phase of the eigenvector, $\vec{e}_\kappa \rightarrow e^{i\phi}\vec{e}_\kappa$. This result is not unexpected since the structure factor in the incommensurate phase is invariant under this transformation. Although our data do not determine a phase Holy *et al.*[12] have shown that when $\phi = -\frac{1}{2}\pi$ the inversion symmetry of the resulting displacement pattern leads to certain Raman selection rules which are observed. In Fig. 9 we illustrate the atomic arrangement generated by this choice of phase.

As mentioned earlier we have observed superlattice peaks in $TaSe_2$ at the points designated by crosses in Fig. 6. These points are characterized by wave vectors of the type $\vec{Q} = (\vec{q}_i - \vec{q}_j) + \vec{G}$, where $(i,j) = (1,2)$, $(2,3)$ or $(3,1)$ and $\vec{G}$ is a $2H$ reciprocal lattice vector. Three possible mechanisms for scattering at these wave vectors are (i) multiple scattering from primary displacement waves, (ii) higher-order diffraction from primary displacement waves, and (iii) an additional displacement wave having the appropriate wave vector.[13] We have measured the temperature dependence of such a peak and the results are shown in Fig. 10. The intensity is much too large to be a multiple-scattering effect. Furthermore, the intensity caused by double scattering (the most probable multiple process) should scale as the square of a primary peak intensity, whereas Fig. 10 indicates at least a third-power variation. It is only necessary to eliminate multiple scattering as the source of this intensity in order to draw the conclusion that the CDW is a triple-$\vec{q}$ state, since both mechanisms (ii) and (iii) require the simultaneous presence of at least two primary waves in a crystal domain.

In summary, we find that the atomic displacements which describe the commensurate phase of $TaSe_2$ are of Σ_1 symmetry. The motion is predominantly longitudinal with opposing Se and Ta displacements; some transverse displacement of Se atoms in the c-axis direction also occurs. There is a reasonably large phase difference between transition-metal motion in the two fundamental layers. Furthermore, the evidence suggests that a model containing three symmetry-equivalent waves, a triple-$\vec{q}$ state, describes the CDW in $TaSe_2$. Finally, we reiterate that although extensive measurements have not been carried out on $NbSe_2$, this compound does exhibit a similar distribution of superlattice intensities, although they

TABLE I. Magnitudes and phases of the independent components of $\vec{e}_\kappa(\vec{q}_1)$ derived from superlattice structure factor data on $TaSe_2$ at 5 K. The remaining components are related to these by Eq. (A10). Errors quoted are one-standard-deviation values associated with the goodness of fit.

Magnitudes (Å)	Phases (rad)
$\epsilon^1_{1x} = -0.048$ (1)	$\phi^1_{1x} = -0.80$ (3)
$\epsilon^1_{3x} = 0.009$ (1)	$\phi^1_{3x} = 0.36$ (9)
$\epsilon^1_{3z} = -0.0172$ (5)	$\phi^1_{3z} = -0.28$ (6)

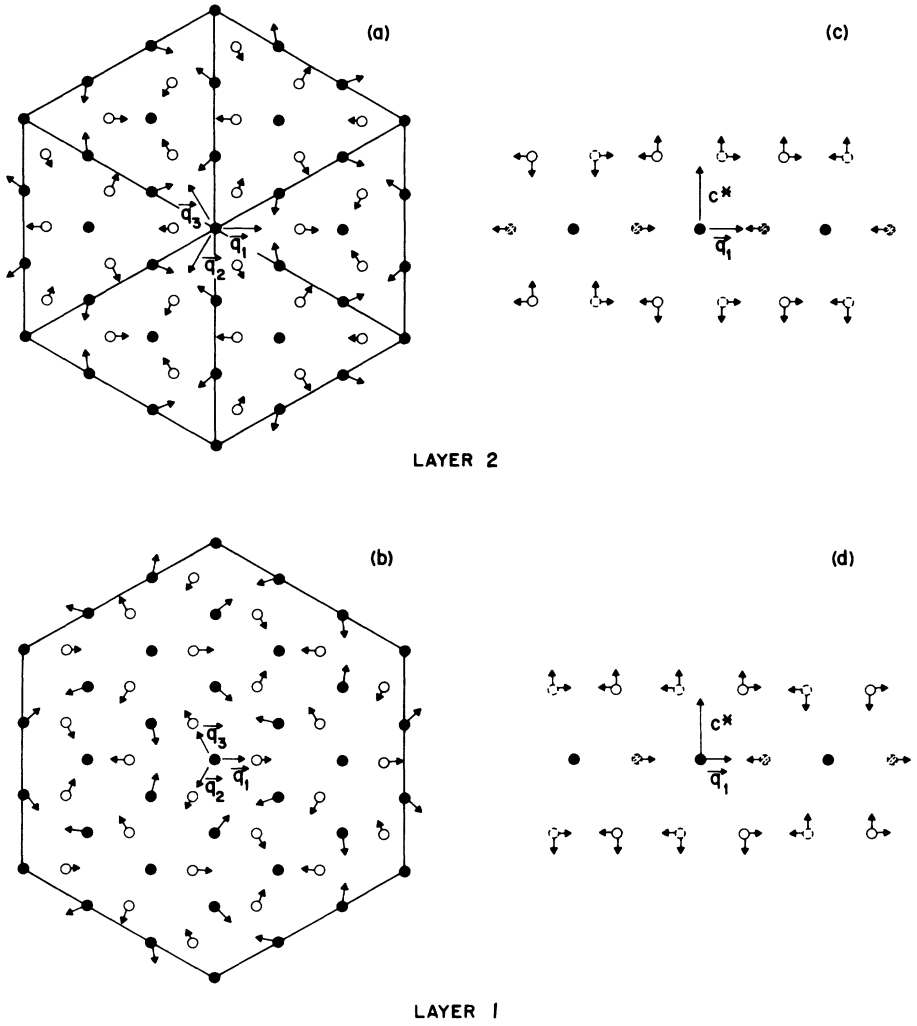

FIG. 9. Schematic view of the displacement pattern for $TaSe_2$ at 5 K. Basal plane projections of the structure for the two layers are shown in (a) and (b); projections on the $(h0l)$ plane are given in (c) and (d). Arrow lengths are exaggerated and relative magnitudes are only suggestive of the proper values.

are generally weaker relative to the main Bragg peaks. Therefore, the atomic displacements must be smaller than in $TaSe_2$ as would be expected with a lower T_0.

IV. INELASTIC-SCATTERING RESULTS

A. Phonon dispersion at 300 K

We have studied most of the phonon branches having energies below 12 meV along the $[\zeta 00]$ and $[00\zeta]$ directions in both compounds at 300 K. In general, neutron groups were collected using the constant-$\vec{Q}$ method, and the energy transfer associated with a particular group was determined graphically. The various branches are classified according to their group theoretical representations. The analysis in the Appendix shows that modes with $[\zeta 00]$ propagation vectors have four irreducible representations (Σ_1, Σ_2, Σ_3, and Σ_4), all of which are nondegenerate. Of the 18 branches, there are six Σ_1's, two Σ_2's, six Σ_3's, and four Σ_4's. Table V shows that the eigenvectors of Σ_2 and Σ_4 symmetry involve purely transverse atomic motion, while Σ_1 is predominantly longitudinal and Σ_3 is predominantly transverse. Analysis of modes along $\Delta[00\zeta]$ yields two nondegenerate representations (Δ_1 and Δ_2), containing three branches each, and two doubly-degenerate representations (Δ_5 and Δ_6), containing six branches each. These modes are purely transverse (Δ_6 and Δ_5), or purely longitudinal (Δ_1 and Δ_2).

The dispersion curves with the exception of the Σ_1 branch are shown in Fig. 11 for $TaSe_2$ and Fig. 12 for $NbSe_2$. Some part of each of the low-lying

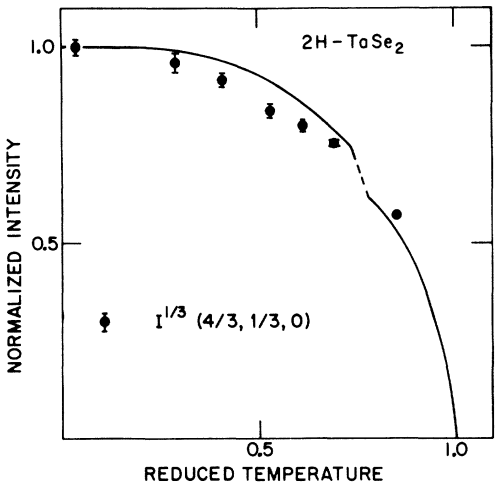

FIG. 10. Normalized intensity of the $(\frac{4}{3}\frac{1}{3}0)$ superlattice peak. Solid curve (data from Fig. 5) represents the intensity of the primary superlattice peaks.

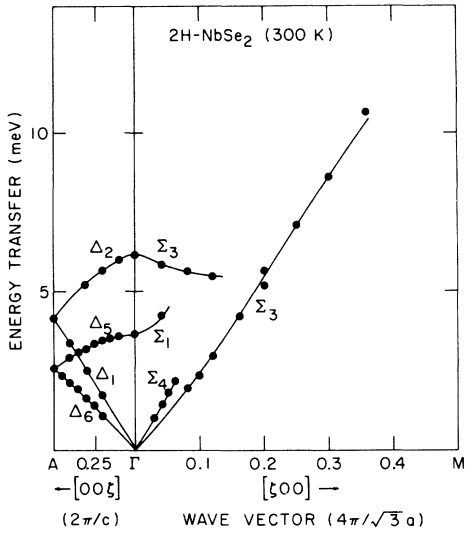

FIG. 12. Dispersion relations for $NbSe_2$ along the [00ζ] and [ζ00] directions.

branches has been observed. We note that modes of Σ_2 symmetry which involve opposing motion of the Se atoms within a single layer were not seen. Apparently, they have higher energies than the branches studied in these experiments. The low energy of the Δ modes is due to the weak interlayer forces. Other features in the dispersion curves of these compounds include the convex curvature of the Σ_3 mode and its isotropy in the basal plane, indicated by the [ζζ0] data for $TaSe_2$ shown in Fig. 11. This mode would have purely quadratic dispersion in the absence of the interlayer force.

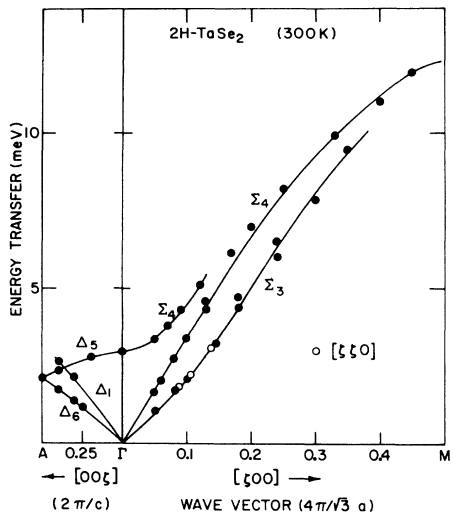

FIG. 11. Dispersion relations for $TaSe_2$ along the [00ζ] and [ζ00] directions. Some data along [ζζ0] are also shown scaled in units of $Å^{-1}$.

Similar convexity and basal plane isotropy have been observed in studies of pyrolytic graphite,[14] MoS_2,[15] and $NbSe_2$.[16]

Although the size of the resolution function prohibits the measurement of acoustic mode dispersion close to the zone center, crude estimates of the slope have been made from the available data. These results are shown in Table II for various branches and the calculated elastic constants are given. We emphasize that these elastic constants are zero-sound constants which are not strictly equivalent to the hydrodynamic elastic constants.

Although the layered structure alone causes interesting lattice-dynamical effects, the influence of the conduction electrons is our main concern here. These effects are most pronounced on the Σ_1 modes shown in Fig. 13. Striking softening of these modes is evident for wave vectors given by $\zeta > 0.2$ in both compounds. The pronounced anomaly in the vicinity of $\zeta = 0.33$ is insensitive to the c-axis component of momentum transfer, implying a strong two-dimensional character. This fact is demonstrated in Fig. 14 which compares scans at $\vec{Q} = (3+\zeta, 0, 0)$ with those taken at $\vec{Q} = (3+\zeta, 0, 0.5)$.

The work of Wakabayashi *et al.*[15] on the semiconductor MoS_2 helps demonstrate that the mode softening in the metallic compounds is due to the conduction electrons. MoS_2 has a $2H$ structure similar to $TaSe_2$ and $NbSe_2$, but since it is a semiconductor there are no conduction-electron effects. The dispersion curves of MoS_2 (including branches up to 60 meV) can be fit with a conventional lattice-dynamics model, including force constants for the bending and stretching of Mo–S bonds and an axially symmetric S–S interlayer force. Although Waka-

TABLE II. Zero-sound elastic constants for $TaSe_2$ and $NbSe_2$ at 300 K.

Mode	Elastic constant	Slope (meV Å) $TaSe_2$	Slope (meV Å) $NbSe_2$	Velocity (10^4 cm/sec) $TaSe_2$	Velocity (10^4 cm/sec) $NbSe_2$
Σ_1	C_{11}	34 (2)	36 (8)	51.5 (30)	55 (12)
Σ_3	C_{44}	9.1 (7)	9.8 (7)	13.8 (11)	14.9 (11)
Σ_4	$1/2(C_{11}-C_{12})$	17.5 (15)	18.5 (18)	26.6 (23)	28.1 (27)
Δ_1	C_{33}	16.4 (6)	16.7 (8)	24.9 (9)	25.4 (12)
Δ_6	C_{44}	9.8 (4)	11.2 (4)	14.9 (6)	17.0 (6)

Elastic constant (10^{11} dyn/cm^2)	$TaSe_2$	$NbSe_2$
C_{11}	22.9 (27)	19.4 (80)
C_{12}	10.7 (31)	9.1 (88)
C_{33}	5.4 (4)	4.2 (4)
C_{44}	1.85 (13)	1.76 (13)

bayashi *et al.* saw some need for including atomic polarizability effects, the dispersion curves are fairly well characterized without them. Using the bond and layer force constants which describe the best fit to the MoS_2 data, and scaling the masses properly, Wakabayashi *et al.*[16] calculated dispersion curves for $NbSe_2$. Their measurements on $NbSe_2$ (5% Mo) show that, although the $[00\zeta]$ modes and the $[\zeta 00]$ acoustic velocities are well predicted by this "semiconductor" model, the measured Σ_1 and Σ_3 modes fall considerably lower in energy for $\zeta > 0.2$. This comparison provides convincing evidence of the presence of strong interactions between the phonons and the conduction electrons.

The data of Fig. 13 show, in addition to the general softening, a pronounced dip in the Σ_1 branch of $TaSe_2$ near $\vec{q}_c$ (i.e., $\zeta = 0.33$). Since (i) this vector is characteristic of the low-temperature CDW superlattice, and (ii) we have found that the atomic displacements involved in CDW formation have the Σ_1 symmetry (see Sec. III B), it is clear that this phonon branch is of key importance in the CDW transition. In Fig. 15 we show typical neutron groups from the $TaSe_2$ Σ_1 mode (Fig. 13). The ob-

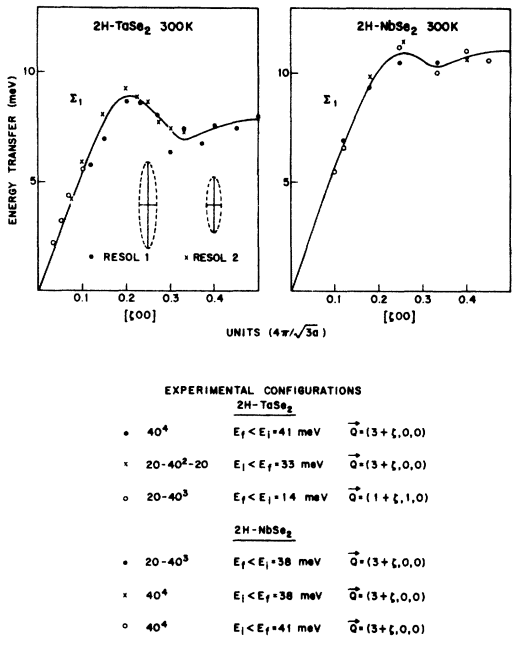

FIG. 13. Dispersion relations for the Σ_1 phonon branches in $TaSe_2$ and $NbSe_2$.

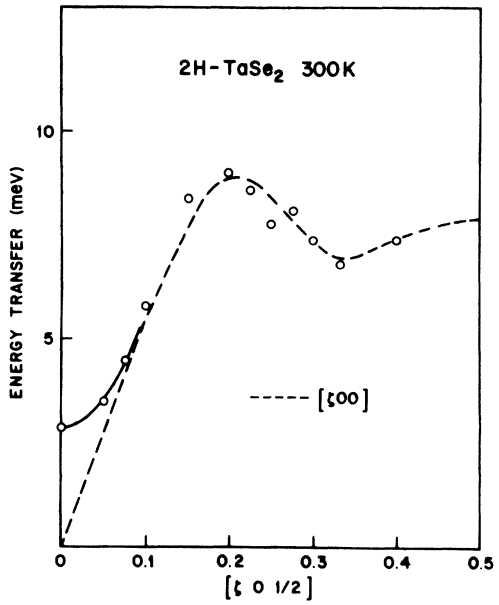

FIG. 14. Phonon dispersion relations along $[\zeta 00]$ and $[\zeta 0\frac{1}{2}]$ show the two-dimensional character of the softening near at $\zeta = 0.33$.

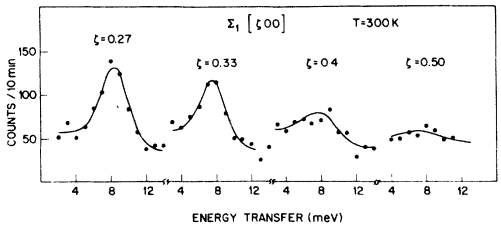

FIG. 15. Neutron groups for the $\Sigma_1[\zeta 00]$ branch. The intensity diminishes as ζ increases as a result of changes in the phonon eigenvector.

served neutron groups have a large instrumental energy width, since the data were obtained using resolution 1 (Fig. 13). In addition to revealing the shape of the dispersion relation, these data provide evidence of a rapidly varying phonon eigenvector. The rapid decrease in phonon intensity in going from $\zeta = 0.27$ to $\zeta = 0.5$ cannot be explained by either the small variation in phonon energy or the $\vec{Q}$ dependence of a simple acoustic structure factor. We suggest that this variation is connected with the effects of the conduction electrons. This interpretation is consistent with the fact that Wakabayashi[17] has not observed such behavior in MoS_2.

B. Lattice-dynamical effects near the CDW transition temperatures

Despite the weak intensities resulting from small sample volume, we have made a limited study of the temperature dependence of the lattice dynamics of $TaSe_2$. Our examination has involved only excitations of Σ_1 symmetry. Experimentally, we have approached these measurements from two directions.

First, using an incident beam energy of 14 meV and collimation of $(40)^4$ we have studied the evolution of quasielastic critical scattering at temperature near T_0. These experiments have centered around reciprocal lattice points which are characterized by strong elastic scattering from the CDW superlattice below T_0 [i.e., near $\vec{Q} = (\frac{5}{3}, 0, 0)$ and $(\frac{4}{3}, 0, 0)$].

Second, using an incident beam energy of 33 meV and collimation of 20-40-40-20 (resolution 2 of Fig. 13) we have followed the Σ_1 mode as a function of temperature. This mode has predominantly longitudinal character at small $\vec{q}$, so the phonon cross-section is largest near strong Bragg peaks of the $2H$ phase. Since the (300) peak is the strongest $(h00)$ peak, these measurements were made with $\vec{Q} = (3 + \zeta, 0, 0)$ where $0 < \zeta < 0.5$. We will now discuss the data obtained from these two approaches.

The critical scattering intensity distribution in reciprocal space above T_0 is similar to that of the superlattice Bragg scattering below T_0. Therefore, the fluctuations must involve atomic displacements characteristic of the CDW state. We find that the critical scattering has a reduced wave vector $\vec{q}_0 = (\frac{1}{3}(1 - \delta_0), 0, 0)$ which is essentially independent of temperature between 140 K and $T_0 = 122.3$ K. The superlattice Bragg peaks develop at $\vec{q}_0$, but shift rapidly toward commensurability as the CDW grows below T_0. This result suggests that the temperature dependence of the superlattice wave vector $\vec{q}_0$ is induced by the growth of the CDW rather than by an intrinsic temperature dependence of $\vec{q}_0$.

Figure 16 shows the critical scattering evident at the $(\frac{1}{3}(5 + \delta_0), 0, 0)$ superlattice point. The apparent energy width is accounted for by the spectrometer resolution at all temperatures. We have integrated the intensity over energy and plotted its inverse against temperature. Within simple mean-field theory, a $(T - T_0)$ dependence is expected. The results are in agreement with a linear relation, however, the value of T_0 obtained is 119.8 K. We expect that resolution corrections would raise this temperature, but it is also possible that the transition is weakly first order. In such a case the superlattice forms above the temperature at which the fluctuations would appear to diverge.

Since CDW formation in these materials is related to the anisotropy of the layered structure, one expects that the forces which act to develop long-range order will exhibit anisotropy as well. This is observed in the $E = 0$ scans shown in Fig. 17. At 123 K the inverse correlation length in the plane, $\kappa_{\parallel}$, is about one-third of the value found for $\kappa_{\perp}$. This result demonstrates that $2H$-$TaSe_2$ is not unusually two-dimensional. There are two-dimensional magnetic systems with critical scattering intensity *independent* of the c-axis momentum

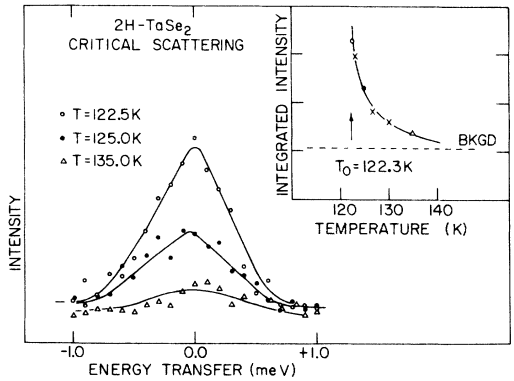

FIG. 16. Critical scattering in $2H$-$TaSe_2$ at $\vec{Q} = ((5 + \delta_0)/3, 0, 0)$. The energy width is characteristic of the spectrometer resolution. Inset shows the integrated intensity of the critical scattering versus temperature.

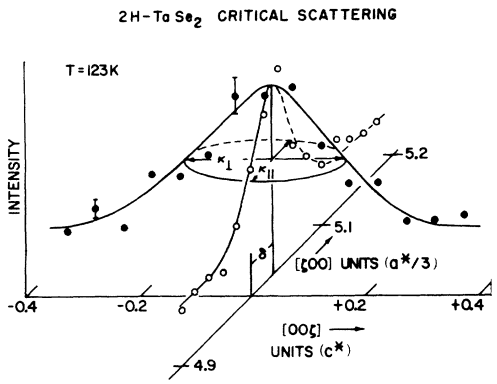

FIG. 17. Critical scattering at $\vec{Q}=((5+\delta_0)/3,0,0)$. These $E=0$ scans show anisotropic correlation lengths. $\kappa_{\parallel}$ and $\kappa_{\perp}$ differ by a factor of 3.

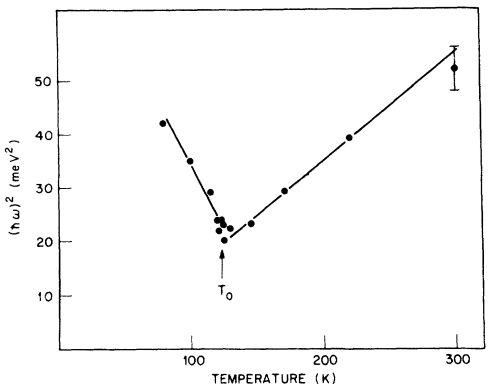

FIG. 19. Temperature dependence of the phonon energy ($\hbar\omega$) taken from a series of scans such as that in Fig. 18. The energy is minimized at the temperature T_0 where the CDW superlattice forms.

transfer.[18]

Constant-$\vec{Q}$ scans such as those shown in Fig. 16 have been extended to higher energies (up to 8 meV), but it has not been possible to locate a phonon peak. However, the larger resolution function obtained with a higher incident energy and larger momentum transfers allows the measurement of the Σ_1 branch, as demonstrated in Sec. III (Fig. 13). Low-temperature scans obtained at $\vec{Q}=(3.33,0,0)$ with resolution 2 (Fig. 13) reveal a phonon peak with a frequency which decreases on approaching T_0. A typical scan taken at 125 K is shown in Fig. 18. In addition to the peak at finite frequency, a weak quasielastic central peak develops below about 150 K with intensity increasing toward T_0. This central component is equivalent to the critical scattering discussed above.

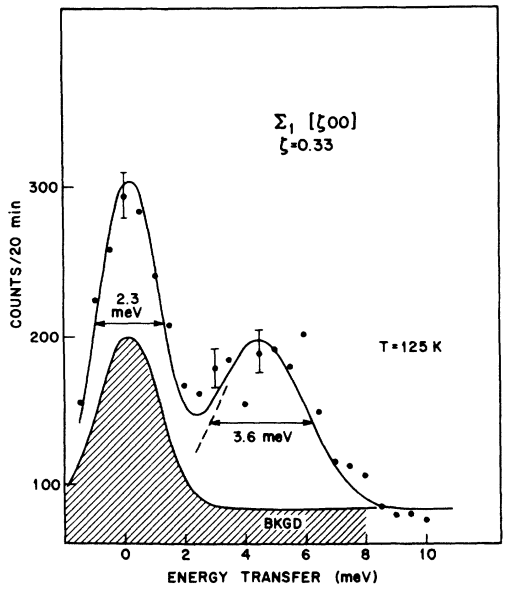

FIG. 18. Constant-$\vec{Q}$ scan of the $\Sigma_1[\zeta 00]$ branch at $\zeta=0.33$. These data taken at 125 K show both a resolution-limited central component and a broader phonon peak at finite energy.

Although we have a set of scans such as that shown in Fig. 18 at many temperatures, two important complications prevent a detailed analysis. First, the size of our resolution function takes an average over such a large portion of the dispersion surface that a sharp anomaly would be severely distorted in both its energy and wave-vector dependence. Second, the rapid reduction in the Σ_1 phonon structure factor implied by the data of Fig. 15 heavily weights the smaller wave vector phonons in scans taken at nominal momentum transfers near $\zeta=0.33$. It is not possible to analyze the data taking these complications properly into account. Therefore, we have simply plotted the square of the frequency associated with the phonon peak versus temperature in Fig. 19 in order to demonstrate the significant temperature dependence of this mode and establish its direct relation to the CDW transition at T_0. We emphasize, however, that these data may not be an accurate quantitative characterization of the Σ_1 mode at the critical wave vector due to the difficulties discussed above.

V. THEORETICAL CONSIDERATIONS

A. Development of a Landau theory

It is possible to interpret many features of these CDW phase transitions with the use of a Landau free-energy expansion. In spite of many simplifying assumptions, such free-energy expansions have been successful in relating experiment to theory for many second-order phase transitions.

In constructing the free-energy we follow Landau[19] by expanding in terms of order parameters. Since the CDW transition involves the formation of a lattice distortion, its amplitude is a natural choice for the order parameter. On the other hand, it is possible to consider the charge density as the order parameter, as has been done recently by McMillan.[20] Since CDW formation involves a *linear* coupling between the charge density and the lattice distortion, the two quantities are simply proportional to one another. Consequently, the free energy may be expressed in terms of either electronic or nuclear coordinates. In either case, the coefficients include important contributions from both the electrons and the lattice. Since the experimental results we have presented deal entirely with the measurement of lattice properties, we choose the order parameter to be the lattice distortion.

A general distortion displaces the κth atom in the lth unit cell by an amount

$$\vec{u}_{l\kappa} = \sum_{\vec{q}} Q_{\vec{q}} \vec{\xi}_{\kappa}(\vec{q}) e^{i\vec{q}\cdot\vec{R}_l} , \tag{5.1}$$

where the $Q_{\vec{q}}$ are complex amplitudes and the $\vec{\xi}_{\kappa}(\vec{q})$ are suitably normalized eigenvectors. The phonon branch index is suppressed since we will be concerned only with modes of Σ_1 symmetry. These quantities are related to the eigenvector $\vec{e}_{\kappa}(\vec{q})$, used in Sec. III B via the relation

$$\vec{e}_{\kappa}(\vec{q}) = Q_{\vec{q}} \vec{\xi}_{\kappa}(\vec{q}) .$$

Here

$$Q_{-\vec{q}} = Q_{\vec{q}}^{*} \tag{5.2}$$

insures that the displacements $\vec{u}_{l\kappa}$ are real.

Following Kwok and Miller[21] we expand the free energy in the following form:

$$F = F_0 + \frac{1}{2!} \sum_{\vec{q},\vec{q}'} A(\vec{q},\vec{q}') Q_{\vec{q}} Q_{\vec{q}'} \Delta(\vec{q}+\vec{q}') + \frac{1}{3!} \sum_{\vec{q},\vec{q}',\vec{q}''} B(\vec{q},\vec{q}',\vec{q}'') Q_{\vec{q}} Q_{\vec{q}'} Q_{\vec{q}''} \Delta(\vec{q}+\vec{q}'+\vec{q}'')$$
$$+ \frac{1}{4!} \sum_{\vec{q},\vec{q}',\vec{q}'',\vec{q}'''} C(\vec{q},\vec{q}',\vec{q}'',\vec{q}''') Q_{\vec{q}} Q_{\vec{q}'} Q_{\vec{q}''} Q_{\vec{q}'''} \Delta(\vec{q}+\vec{q}'+\vec{q}''+\vec{q}''') , \tag{5.3}$$

where F_0 is the free-energy of the undistorted structure, and the function $\Delta(\vec{q})$ is defined by

$$\Delta(\vec{q}) = \begin{cases} 1 & \text{if } \vec{q} = \vec{G} \\ 0 & \text{otherwise} \end{cases} .$$

The Δ-function guarantees that terms which contribute to F are invariant under the translation operations of the high-symmetry structure. The coefficients in the free energy are the Fourier transforms of the terms that occur when the general lattice potential is expanded in a Taylor series in the atomic displacements $\vec{u}_{l\kappa}$. Without loss of generality, A and C may be taken to be real, whereas B is purely imaginary.

The harmonic terms can be written

$$\frac{1}{2} \sum_{\vec{q},\vec{q}'} A(\vec{q},\vec{q}') Q_{\vec{q}} Q_{\vec{q}'} \Delta(\vec{q}+\vec{q}') = \frac{1}{2} \sum_{\vec{q}} A(\vec{q}) Q_{\vec{q}} Q_{-\vec{q}} , \tag{5.4}$$

where $A(\vec{q}) \equiv A(\vec{q}, -\vec{q})$. Stability of the high-temperature phase requires both A and C to be positive for all $\vec{q}$. A phase transition occurs when A becomes negative as a function of temperature for some value of $\vec{q}$. We assume

$$A(\vec{q}, T) = \alpha(T - T_0) + |\vec{q} - \vec{q}_0|^2 . \tag{5.5}$$

This simple form for $A(\vec{q}, T)$ will produce a lattice distortion at $T = T_0$ having an incommensurate wave vector with magnitude $q_0 = \frac{1}{3}(1 - \delta_0)a^*$, where δ_0 is a temperature-independent constant. Further, we will assume that both B and C are temperature-independent constants.

Now we consider the free energy of a lattice distortion of wave vector $\vec{q}_\delta = (1 - \delta)\vec{q}_c$. Here δ is a variable whose temperature dependence we wish to determine (if $\delta = 0$, the superlattice is commensurate with wave vector $\vec{q}_c$). We assume a single-$\vec{q}$ CDW. This state is stable if one neglects coupling terms between the three waves in a triple-$\vec{q}$ configuration. Consider first the harmonic term. A distortion of wave vector $\vec{q}_\delta$ contributes a term

$$A(\vec{q}_\delta, T) Q_{\vec{q}_\delta} Q_{-\vec{q}_\delta} = A(\vec{q}_\delta, T) \eta_\delta^2 , \tag{5.6}$$

to the free energy. Here we have expressed $Q_{\vec{q}_\delta}$ in terms of a real amplitude and phase,

$$Q_{\vec{q}_\delta} = \eta_\delta e^{i\alpha_\delta} , \tag{5.7}$$

and made use of Eq. (5.2). A similar term $A(\vec{q}_c, T)\eta_c^2$ represents the harmonic energy of a commensurate wave.

We now examine the third-order terms in Eq. (5.3). Unlike the harmonic term, the third-order term is distinctly different for the commensurate ($\delta = 0$) and incommensurate ($\delta \neq 0$) waves. For $\delta = 0$ we can satisfy the requirement $\vec{q} + \vec{q}' + \vec{q}'' = \vec{G}$ by the choice $\vec{q} = \vec{q}' = \vec{q}'' = \vec{q}_c$, thereby generating the umklapp term

$$\tfrac{1}{3}|B|\eta_c^3 \sin(3\alpha_c). \tag{5.8}$$

It is always possible to choose the phase α_c such that $\sin(3\alpha_c) = -1$. The lowest free energy then has the third-order term $-\frac{1}{3}|B|\eta_c^3$. For the incommensurate wave, there is no term proportional to η_δ^3, because the Δ function vanishes. However, coupling terms of the form

$$(1/3!)BQ_{\vec{q}_\delta}^2 Q_{\vec{G}-2\vec{q}_\delta}$$

are allowed. Here we have introduced a secondary lattice distortion of wave vector

$$\vec{G} - 2\vec{q}_\delta = \tfrac{1}{3}(1+2\delta)\vec{a}^* \equiv \vec{q}_{2\delta}.$$

Counting all the equivalent terms properly, and substituting amplitudes and phases, we obtain

$$|B|\eta_\delta^2\eta_{2\delta}\sin(2\alpha_\delta + \alpha_{2\delta}). \tag{5.9}$$

Again choosing α_δ and $\alpha_{2\delta}$ such that $\sin(2\alpha_\delta + \alpha_{2\delta}) = -1$, we find that this third-order term lowers the free energy if waves of both wave vector $\vec{q}_\delta$ and $\vec{q}_{2\delta}$ exist in the crystal. The secondary wave also contributes a positive harmonic term $A(\vec{q}_{2\delta}, T)\eta_{2\delta}^2$ to the free energy.

In taking the free-energy expansion to fourth order, we must include a term $\frac{1}{4}C\eta_c^4$ for the commensurate wave. For the incommensurate case there are three fourth-order terms

$$\tfrac{1}{4}C(\eta_\delta^4 + \eta_{2\delta}^4) + C\eta_\delta^2\eta_{2\delta}^2.$$

Note that the phases of the waves do not enter the fourth-order terms. Therefore, we were justified in assuming the freedom to minimize the third-order terms. Collecting terms gives the following expressions for the free energy of the commensurate and incommensurate states:

$$F_{\rm com}(\vec{q}_c) = A(\vec{q}_c, T)\eta_c^2 - \tfrac{1}{3}B\eta_c^3 + \tfrac{1}{4}C\eta_c^4, \tag{5.10}$$

$$F_{\rm inc}(\vec{q}_\delta) = A(\vec{q}_\delta, T)\eta_\delta^2 + A(\vec{q}_{2\delta}, T)\eta_{2\delta}^2 - B\eta_\delta^2\eta_{2\delta} + \tfrac{1}{4}C(\eta_\delta^4 + \eta_{2\delta}^4) + C\eta_\delta^2\eta_{2\delta}^2 \tag{5.11}$$

In Sec. V B we will discuss the behavior of these free energies as a function of temperature, and compare predictions with the experimental data.

Next, we briefly consider the form of the free energy which will describe a CDW with three simultaneous displacement waves with wave vectors $\vec{q}_1$, $\vec{q}_2$, and $\vec{q}_3$. If the CDW is commensurate, we find

$$\begin{aligned} F_{\rm com}(\vec{q}_1,\vec{q}_2,\vec{q}_3) = {} & F_{\rm com}(\vec{q}_1) + F_{\rm com}(\vec{q}_2) + F_{\rm com}(\vec{q}_3) + B'(Q_{\vec{q}_1}Q_{\vec{q}_2}Q_{\vec{q}_3} + \text{c.c.}) \\ & + C'(|Q_{\vec{q}_1}|^2|Q_{\vec{q}_2}|^2 + |Q_{\vec{q}_2}|^2|Q_{\vec{q}_3}|^2 + |Q_{\vec{q}_1}|^2|Q_{\vec{q}_3}|^2) \\ & + C''[(Q_{\vec{q}_1}^2 Q_{-\vec{q}_2}Q_{-\vec{q}_3} + Q_{\vec{q}_2}^2 Q_{-\vec{q}_1}Q_{-\vec{q}_3} + Q_{\vec{q}_3}^2 Q_{-\vec{q}_2}Q_{-\vec{q}_1}) + \text{c.c.}], \end{aligned}$$

where c.c. means complex conjugate. This free energy can be used to show that a two-$\vec{q}$ state is not energetically favorable. We look for extrema of the function by setting

$$\frac{\partial F_{\rm com}}{\partial Q_{\vec{q}_i}} = \frac{\partial F_{\rm com}}{\partial Q_{-\vec{q}_i}} = 0, \quad i = 1,2,3.$$

We substitute

$$Q_{\vec{q}_i} = \eta_i e^{i\alpha_i},$$

and set $\eta_1 = \eta_2$ and $\eta_3 = 0$, corresponding to a two-$\vec{q}$ state. The resulting equations cannot be satisfied for general coefficients A, B, C, B', C', C''. Therefore, we conclude that a two-$\vec{q}$ CDW does not minimize the free energy. A similar analysis shows that single-$\vec{q}$ and triple-$\vec{q}$ states are possible.

In the incommensurate triple-$\vec{q}$ state, there are no fourth-order umklapp coupling terms similar to those in $F_{\rm com}(\vec{q}_1,\vec{q}_2,\vec{q}_3)$. However, there is a third-order term $B'Q_{\vec{q}_1}Q_{\vec{q}_2}Q_{\vec{q}_3}$ coupling the three waves. Its presence results in a first-order phase transition above T_0. Since the CDW in $TaSe_2$ appears to be a triple-$\vec{q}$ state (see Sec. III B), the absence of experimental evidence of first-order behavior implies that this coupling term must be weak. This result increases our confidence in the use of the single-$\vec{q}$ free-energy to understand the behavior of these materials.

B. Comparison with the data

Although we believe that a triple-$\vec{q}$ CDW exists in these materials, the single-$\vec{q}$ free-energies [Eqs. (5.10 and 5.11)] are considerably simpler. They contain the essential terms which explain the existence of the secondary lattice distortion, the temperature dependence of $\vec{q}_\delta$, and the lock-in transition. We will develop approximate expressions and numerical solutions for the temperature dependence of the variables (η_c, or η_δ, $\eta_{2\delta}$, and $\vec{q}_\delta$) which minimize these free energies and compare them with the $TaSe_2$ data.

First, we consider the incommensurate state described by $F_{\rm inc}$. Minimizing with respect to η_δ and $\eta_{2\delta}$ gives the equations

$$\frac{\partial F_{\rm inc}}{\partial \eta_\delta} = 2A(\vec{q}_\delta, T)\eta_\delta - 2B\eta_\delta\eta_{2\delta} + C\eta_\delta^3 + 2C\eta_\delta\eta_{2\delta}^2 = 0, \tag{5.12}$$

$$\frac{\partial F_{\rm inc}}{\partial \eta_{2\delta}} = 2A(\vec{q}_{2\delta}, T)\eta_{2\delta} - B\eta_\delta^2 + C\eta_{2\delta}^3 + 2C\eta_\delta^2\eta_{2\delta} = 0. \tag{5.13}$$

We will keep only those terms in the above equations of order η_δ^4. Equation (5.13) implies that $\eta_{2\delta} \propto \eta_\delta^2$ if these quantities are small. Therefore, we discard the $C\eta_{2\delta}^3$ term from Eq. (5.13) since it is of order η_δ^6, and find

$$\eta_{2\delta}(T) = B\eta_\delta^2(T)/[2A(\vec{q}_{2\delta}, T) + 2C\eta_\delta^2(T)]. \tag{5.14}$$

Substituting this result into Eq. (5.12), and solving for η_δ gives

$$\eta_\delta(T) = -2A(\vec{q}_\delta, T)/[C - B^2/A(\vec{q}_{2\delta}, T)]. \tag{5.15}$$

The above expressions minimize $F_{\rm inc}$ when $A(\vec{q}_\delta, T) \leq 0$. For $A(\vec{q}_\delta, T) > 0$, the undistorted state, $\eta_\delta = \eta_{2\delta} = 0$, has lower free energy. Therefore, at T_0 the primary wave begins to form at wave vector $\vec{q}_\delta = \vec{q}_0$ (i.e., $\delta = \delta_0$), in a second-order transition with $\eta_\delta(T)$ increasing as $(T_0 - T)^{1/2}$. In addition, a secondary wave grows with magnitude $\eta_{2\delta}(T)$ proportional to $\eta_\delta^2(T)$. Although the primary wave forms at $\delta = \delta_0$, the value of $\delta(T)$ below T_0 is strong strongly temperature dependent. To see this effect we substitute the solutions for η_δ and $\eta_{2\delta}$ into $F_{\rm inc}$ and minimize it with respect to δ. For $F_{\rm inc}$ we obtain

$$F_{\rm inc}(T) = -A^2(\vec{q}_\delta, T)/[C - B^2/A(\vec{q}_{2\delta}, T)]. \tag{5.16}$$

Using the condition

$$\frac{\partial F_{\rm inc}}{\partial \delta} = 0,$$

we find that,

$$\delta(T) = \delta_0 + \gamma\alpha(T - T_0), \tag{5.17}$$

to first order in $(T - T_0)$. Here $\gamma = B^2/27\delta_0^3 C$. This shows explicitly that the primary wave first develops at $\delta = \delta_0$, but that δ *decreases* (i.e., the wave vector approaches $\vec{q}_c$ linearly with decreasing temperature. This effect vanishes in the absence of the coupling term $-B\eta_\delta^2\eta_{2\delta}$, since $\gamma = 0$ if $B = 0$. In the present materials δ_0 is very small, $\simeq 0.025$ [see Fig. 4(a)] which can result in a large γ even for a small coupling constant B. Figure 20 is helpful in further understanding this wave vector "pulling" effect. We show the coefficient, $A(\vec{q}, T)$, which determines the harmonic energies of both the $\vec{q}_\delta$ and the $\vec{q}_{2\delta}$ waves. As the temperature passes through T_0, the primary distortion forms at $\vec{q}_0 = (1 - \delta_0)\vec{q}_c$. At lower temperatures, the secondary distortion at $\vec{q}_{2\delta} = (1 + 2\delta)\vec{q}_c$ becomes increasingly

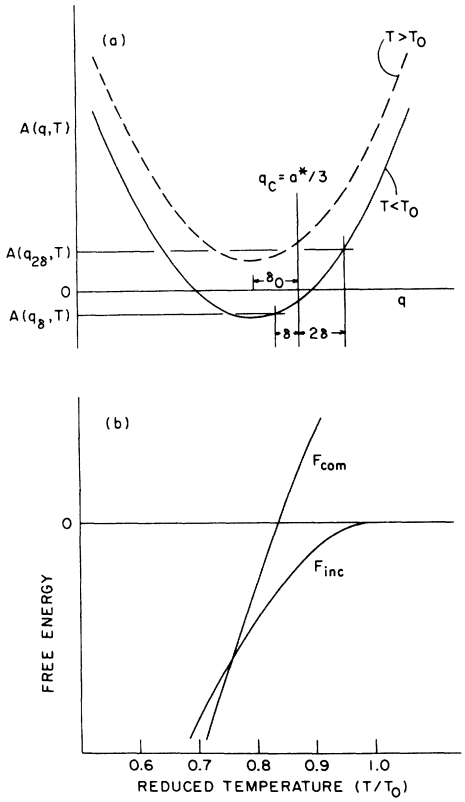

FIG. 20. (a) Coefficient $A(q, T)$ versus wave vector q at temperature above and below T_0. (b) The free-energies $F_{\rm inc}$ and $F_{\rm com}$ versus temperature for the model discussed in text.

costly in harmonic energy, because its magnitude is growing as η_δ^2. If δ is decreased, this energy, $A(\vec{q}_{2\delta}, T)\eta_{2\delta}^2$, can be lowered without significantly reducing the energy gained, $A(\vec{q}_\delta, T)\eta_\delta^2$, by the formation of the primary wave. We believe that this mechanism is responsible for the rapid temperature variation of $\vec{q}_\delta$ in the incommensurate phases of both $NbSe_2$ and $TaSe_2$.

Next, we consider the free energy of a commensurate wave and the possibility of a first-order lock-in transition. We minimize $F_{\rm com}$, given in Eq. (5.10), by setting

$$\frac{\partial F_{\rm com}}{\partial \eta_c} = 0,$$

and obtain the solution

$$\eta_c(T) = \{B + [B^2 - 8CA(\vec{q}_c, T)]^{1/2}/2C\}. \tag{5.18}$$

The wave vector $\vec{q}_c$ associated with this wave is, of course, temperature independent. Equation (5.18) implies a first-order transition from the undistorted to the commensurate state as a result of the cubic term $-\frac{1}{3}B\eta_c^3$. Under what conditions will a transition to the commensurate state occur at or

above T_0? To answer this question we set $F_{com}(\eta_c, T_0) \leq 0$. After some algebra we find $B^2/C \geq 9A(\vec{q}_c, T_0)$. Since $A(\vec{q}_c, T_0) = \delta_0^2$ we have simply $B^2/C \geq 9\delta_0^2$. This criterion is complementary to that necessary for the formation of an incommensurate wave at T_0. Returning to Eq. (5.16), we see that F_{inc} will only be negative just below T_0 if the denominator is positive. The condition is $B^2/C < 9\delta_0^2$, since $A(\vec{q}_{2\delta}, T_0) = 9\delta_0^2$.

In summary, we find two distinct possibilities. If $B^2/C \geq 9\delta_0^2$, a first-order transition occurs at $T_{com} \geq T_0$, to a commensurate ($\vec{q} = \vec{q}_c$) superlattice. If $B^2/C \leq 9\delta_0^2$ a second-order transition occurs to the incommensurate state having a strongly temperature-dependent wave vector. If B^2/C is sufficiently close to $9\delta_0^2$, we expect F_{com} to become lower than F_{com} to become lower than F_{inc} at some temperature below T_0, resulting in a first-order lock-in transition.

Since these simple free energies qualitatively describe the behavior observed in $TaSe_2$, we have attempted to compare their predictions with the experimental curves for $\delta(T)$ and the ratio $\eta_{2\delta}(T)/\eta_\delta(T)$ shown in Figs. 4(a) and 4(c). The parameters needed are α, δ_0, and T_0 [contained in $A(\vec{q}, T)$] and the coefficients B and C. It is evident from Eq. (5.17) that $\delta(T)$ depends on α, δ_0, T_0, and the ratio B^2/C. Using Eqs. (5.14) and (5.15), we find that $\eta_{2\delta}(T)/\eta_\delta(T)$ does not depend on B and C independently, but on the combination B^2/C. From the data of Sec. IIIA, we take $\delta_0 = 0.025$ (units $\frac{1}{3}a^*$) and $T_0 = 122.3$ K. We will have two parameters, α and B^2/C, to vary in generating $\delta(T)$ and $\eta_{2\delta}(T)/\eta_\delta(T)$. To do this efficiently, a simple computer program was written to accurately minimize both F_{inc} and F_{com}. These solutions are valid beyond the range of the approximate analytical solutions, and are limited only by the assumptions made in formulating the free energies. Although we were able to vary B and C independently, we found that the numerical results, like the analytic solutions, depend only on B^2/C and α.

A full set of solutions has been developed over the interesting ranges of B^2/C and α. The curves for $\delta(T)$ and $\eta_{2\delta}(T)/\eta_\delta(T)$ which best describe the data are shown in Figs. 4(b) and 4(d). The parameters used in this solution are $B^2/C = 0.87(9\delta_0^2)$ and $\alpha = 0.8(\delta_0^2/T_0)$. For this case, F_{inc} and F_{com} are shown in Fig. 19(b). It is clear that a quantitatively accurate fit is not achieved; δ does not decrease sufficiently rapidly below T_0. Its rate of change can be increased by making B^2/C larger. However, this modification induces the lock-in transition at a higher temperature and causes a larger discrepancy between the measured and calculated values of δ at lock-in. Another disturbing point is the value of α required to obtain a reasonable fit. We have information on this parameter from critical scattering data. At temperatures above T_0, the integrated critical scattering intensity at wave vector $\vec{q}$ is proportional to

$$\frac{1}{A(\vec{q}, T)} = [\alpha(T - T_0) + |\vec{q} - \vec{q}_0|^2]^{-1}.$$

This is a Lorentzian function with a FWHM of $2[\alpha(T - T_0)]^{1/2}$. The FWHM of the critical scattering (Fig. 17) along $\vec{q} // [\zeta 00]$ is $\kappa_{//} \simeq 2\delta_0$ at $T = 123$ K, giving a value $\alpha = 175(\delta_0^2/T_0)$, if the value $T_0 = 122.3$ K is used. As pointed out in Sec. IV B, the critical scattering at $(\frac{1}{3}(5 + \delta_0), 0, 0)$ appears to diverge at $T_0 = 119.8$ K. Although resolution corrections would tend to increase this temperature, it can be used to set a lower experimental limit $\alpha > 38(\delta_0^2/T_0)$, still a factor ~50 larger than the value $\alpha = 0.8(\delta_0^2/T_0)$ necessary to generate reasonable $\delta(T)$ curves. If we use the experimental value of α, it compresses the temperature scale such that the lock-in transition occurs less than one degree below T_0.

Thus the major difficulty with the model is an overly strong tendency toward the commensurate phase. We do not believe that the use of the triple-$\vec{q}$ state terms would rectify this problem. It is possible that inclusion of a $\vec{q}$ dependence in the coefficients B and C would improve the fit, but no microscopic calculations of this dependence are available.

McMillan[22] has recently given a more detailed discussion of the nonsinusoidal nature of the incommensurate distortions. The physics is as follows. A single plane wave with a wave vector close to $\vec{q}_c$ will have rather large regions over which the lock-in potential is attractive, followed by equally large regions over which the lock-in potential is repulsive. A net attractive interaction can be realized either by modulating the amplitude of the wave, making it larger in the attractive regions or by modulating the phase, locally stretching and shrinking the wavelength of the distortion to produce larger attractive regions.

The solutions discussed above have both phase and amplitude distortion, whereas McMillan finds a lower free energy by creating phase distortions alone. The largest Fourier component has a wave vector $\vec{q}_\delta$ with $\vec{q}_{2\delta}$ the leading correction, but additional higher-order terms produce a qualitative change in the nature of the commensurate-incommensurate transformation. In particular $\vec{q}_\delta(T)$ is predicted to vary smoothly between $\vec{q}_0$ and $\vec{q}_c$, which is not in agreement with our observations. Clearly further work is necessary to resolve these discrepancies and clarify the exact nature of the

incommensurate ground state, but it is clear on both experimental and theoretical grounds that it is considerably more subtle and complex than a single plane-wave distortion.

VI. CONCLUSIONS

Since the CDW transitions in the metallic layered dichalcogenides involve both the electrons and the lattice, many of the physical properties of these materials exhibit unusual behavior. Although the electronic properties show unmistakable, and often drastic, anomalies, the study of their lattice properties via electron and neutron diffraction has provided the key to understanding their behavior.

The present neutron scattering work has shown that $2H$-$NbSe_2$ and $2H$-$TaSe_2$ develop incommensurate superlattices in apparently second-order phase transitions at 33.5 and 122.3 K, respectively. At T_0 the reduced wave-vector characterizing the superlattice in both materials is extremely close to, but not exactly $\frac{1}{3}a^*$. A strong pulling of the superlattice wave vector toward $\frac{1}{3}a^*$ occurs as the temperature is decreased. Commensurability is achieved in $TaSe_2$ at 90 K in a first-order lock-in transition; $NbSe_2$ remains incommensurate above 5 K.

The wave vector at T_0 is believed to be determined by the Fermi surface alone. Below T_0, however, our Landau theory shows that the underlying periodicity of the crystal lattice forces the superlattice toward commensurability as the CDW grows in amplitude. Further, this theory indicates that there is a delicate energy trade off between the commensurate and incommensurate states. It predicts that if the superlattice is incommensurate at T_0, the commensurate state may be adopted at lower temperature, as observed.

In addition to studies of the superlattice, we have investigated the lattice-dynamical properties. Strong anomalies are found in the Σ_1 phonon modes of both $NbSe_2$ and $TaSe_2$. Since this mode involves longitudinal atomic displacements, it is natural to expect it to couple strongly to the electronic charge density fluctuations.

The atomic displacements in the CDW state are "opticlike," involving opposing Se- and Ta-atom motion of Σ_1 symmetry. Therefore, the Σ_1 acoustic modes must mix with Σ_1 optic modes as the transition is approached. This feature may simply reflect the fact that the two different atomic species have opposite charges. Therefore, they move in opposite directions under the Coulomb forces established by the CDW. A further study of the dynamical response of the system will be carried out if larger samples become available.

Incommensurability is a key feature of the CDW transition. There is still much to be learned about its origin and its consequences. The exact features of the Fermi surface which determine the superlattice wave vector $\vec{q}_0$ are unclear in the $2H$ materials. It seems extraordinary that the values of δ [Fig. 4(a)] just below T_0 in both materials are essentially identical.

The observation of secondary lattice distortion has important implications concerning the nature of the incommensurate ground state which have been only partially explored here. Another subject deserving further study is the nature of the excitations of the CDW ground state. When an incommensurate superlattice develops the translational symmetry of the lattice is destroyed in a simple way. Mixing occurs between previously independent normal phonon modes at wave vectors $\vec{k}_+ = \vec{q}_0 + \vec{q}$ and $\vec{k}_- = -\vec{q}_0 + \vec{q}$. Overhauser[11] and McMillan[20] have considered the new vibrational modes of the CDW system. Because the free energy is independent of an arbitrary uniform change in CDW phase, one expects long-wavelength fluctuations to appear as gapless Goldstone modes. Since they involve atomic motion, these excitations are in principle observable via inelastic neutron scattering. We hope that future experiments will help to further develop the current understanding of CDW instabilities and incommensurate structures.

ACKNOWLEDGMENTS

Our work has benefited from conversations with R. A. Cowley, S. H. Liu, W. L. McMillan, D. Mukamel, R. Pynn, G. Shirane, and J. A. Wilson. We thank J. A. Holy and M. V. Klein for communication of their Raman scattering results prior to publication, and R. F. Frindt for the loan of a $NbSe_2$ crystal. One of the authors (D.E.M.) is indebted to C. G. Shull for his support.

APPENDIX: SYMMETRY PROPERTIES OF THE Σ NORMAL MODES

The purpose of this appendix is to examine the symmetry properties of those normal vibrational modes of the $2H$ structure which are pertinent to the understanding of the atomic displacements involved in the CDW transition. Work by Maradudin and co-workers[23,24] and Kovalev[25] provides the foundation necessary for a general treatment of such symmetry properties.

We consider those modes which are characterized by a wave vector lying the Γ-Σ-M direction in the reciprocal lattice, namely, $\vec{q} = (q_x, 0, 0)$. With the exception of the zone boundary, $\vec{q}$

TABLE III. Character table for group C_{2v}.

	E	C_2	σ_h	σ_v
Σ_1	1	1	1	1
Σ_2	1	1	−1	−1
Σ_3	1	−1	−1	1
Σ_4	1	−1	1	−1

$=(\frac{1}{2},0,0)$, the maximal group of such wave vectors is C_{2v}. This group consists of the identity operation E, the C_2 rotation around the Σ axis, and two mirror planes σ_h and σ_v. These planes retain the notation of the full group where the subscripts h and v denote, respectively, horizontal and vertical orientation with respect to the sixfold axis. The character table for the C_{2v} group is given in Table III. There are four one-dimensional representations labeled Σ_1–Σ_4. The displacement of the κth atom in the lth unit cell for a normal mode of wave vector $\vec{q}$ is

$$\vec{u}_{l\kappa}(\vec{q})=\tfrac{1}{2}[\vec{e}_\kappa(\vec{q})e^{i\vec{q}\cdot\vec{R}_l}+\vec{e}^{\,*}_\kappa(\vec{q})\,e^{-i\vec{q}\cdot\vec{R}_l}], \tag{A1}$$

where $\vec{R}_l$ is a real lattice vector; we follow the convention

$$\vec{e}^{\,*}_\kappa(\vec{q})=\vec{e}_\kappa(-\vec{q})\,. \tag{A2}$$

For the $2H$ structure $\kappa=1,\ldots,6$, and therefore the general displacement eigenvector has $3\times6=18$ components. We write it in abbreviated form, suppressing the $\vec{q}$ dependence,

$$\underline{e}^j=(\vec{e}^{\,j}_1;\ldots;\vec{e}^{\,j}_6)$$
$$=(e^j_{1x},e^j_{1y},e^j_{1z};\ldots;e^j_{6x},e^j_{6y},e^j_{6z})\,,$$

where the superscript j denotes the symmetry character $\Sigma_j, j=1,2,3,4$. We are fortunate in the present case to have one-dimensional representations; the transformation law is simply

$$\mathcal{T}(R)\cdot\underline{e}^j=\chi^j(R)\underline{e}^j\,. \tag{A3}$$

The 18×18 matrix $\mathcal{T}(R)$ represents the group operation $R=E$, C_2, σ_h, or σ_v. $\chi^j(R)$ is the character of the operation R in the jth representation. The $\mathcal{T}(R)$ matrices can be derived with the aid of Table IV, which shows how the six atoms and three Cartesian coordinates transform under the operations of C_{2v}. In constructing this table, one must remember that the full group of the $2H$ structure (D^4_{6h}) is nonsymmorphic, and a nonprimitive translation $\vec{\tau}=(0,0,\frac{1}{2})$ must be associated with the operations C_2 and σ_h. The characters of the $\mathcal{T}$ representation are also given in Table IV.

TABLE IV. Transformation properties of atoms $1,\ldots,6$ and Cartesian coordinates x,y,z under the operations of C_{2v} and inversion. Characters for the T representation are also shown.

	E	C_2	σ_h	σ_v	i
1	1	1	1	1	2
2	2	2	2	2	1
3	3	4	4	3	6
4	4	3	3	4	5
5	5	6	6	5	4
6	6	5	5	6	3
x	x	x	x	x	$-x$
y	y	$-y$	y	$-y$	$-y$
z	z	$-z$	$-z$	z	$-z$
$\chi^{\mathcal{T}}(R)$	18	−2	2	6	

Before working out the eigenvectors explicitly, we will determine the number of times a_j which each irreducible representation Σ_j occurs in $\mathcal{T}$. The standard formula from group theory is[26]

$$a_j=\frac{1}{d}\sum_R\chi^{\mathcal{T}}(R)\chi^j(R)\,, \tag{A4}$$

where $d=4$, the dimensionality of C_{2v}. We find the following decomposition:

$$\mathcal{T}=6\Sigma_1+2\Sigma_2+6\Sigma_3+4\Sigma_4\,. \tag{A5}$$

This result implies that of the 18 phonon branches one expects for $\vec{q}$ along Σ, six will have Σ_1 symmetry, two will have Σ_2 symmetry, and so on.

We now use Eq. (A3) to construct the eigenvector for the Σ_1 representation. Since $\chi^1(R)=1$, for all R, the equations generated by Eq. (A3) are

$$\mathcal{T}(E)\cdot\underline{e}^1=\mathcal{T}(C_2)\cdot\underline{e}^1=\mathcal{T}(\sigma_h)\cdot\underline{e}^1=\mathcal{T}(\sigma_v)\cdot\underline{e}^1=\underline{e}^1. \tag{A6}$$

If we let

$$\underline{e}^1=(abc;def;ghk;lmn;pqr;stu)\,,$$

and work out the products $\mathcal{T}(R)\cdot\underline{e}^1$, we find

$$\mathcal{T}(E)\cdot\underline{e}^1=\underline{e}^1\,,$$
$$\mathcal{T}(C_2)\cdot\underline{e}^1=(a-b-c;d-e-f;l-m-n;g-h-k;s-t-u;p-q-r)\,,$$
$$\mathcal{T}(\sigma_h)\cdot\underline{e}^1=(ab-c;de-f;lm-n;gh-k;st-u;pq-r)\,,$$
$$\mathcal{T}(\sigma_v)\cdot\underline{e}^1=(a-bc;d-ef;g-hk;l-mn;p-qr;s-tu)\,.$$

TABLE V. Form of the eigenvector e^j with the transformation properties of Σ_j.

Σ_j	Eigenvector e^j	Number of components
Σ_1	$(a\,0\,0; a^*\,0\,0; g\,0\,k; g\,0\,-k; g^*\,0\,-k^*; g\,0\,k^*)$	6
Σ_2	$(0\,0\,0; 0\,0\,0; 0\,h\,0; 0\,-h\,0; 0\,-h^*\,0; 0\,h^*\,0)$	2
Σ_3	$(0\,0\,c; 0\,0\,c^*; g\,0\,k; -g^*\,0\,k; -g^*\,0\,k^*; g^*\,0\,k^*)$	6
Σ_4	$(0\,b\,0; 0\,b^*\,0; 0\,h\,0; 0\,h\,0; 0\,h^*\,0; 0\,h^*\,0)$	4

The form of $\underline{e}^1$ compatible with Eq. (A6) is

$$\underline{e}^1 = (a00; d00; g0k; g\,0\,-k; p0r; p\,0\,-r)\,. \qquad \text{(A7)}$$

The above components are all complex quantities, resulting in a total of 12 independent eigenvector components. This number can be reduced to six, the number implied by the decomposition performed earlier, if we make use of Eq. (A2). We generate $\underline{e}^1(-\vec{q})$ using[27]

$$\underline{e}^1(-\vec{q}) = -\mathcal{T}(i)\cdot\underline{e}^1(\vec{q})\,, \qquad \text{(A8)}$$

where i is the inversion operator. With the help of Table IV, we evaluate Eq. (A8), and find

$$\underline{e}^1(-\vec{q}) = (\vec{e}^1_2; \vec{e}^1_1; \vec{e}^1_6; \vec{e}^1_5; \vec{e}^1_4; \vec{e}^1_3)\,.$$

Equating this to $\underline{e}^1(\vec{q})^*$ yields the relations

$$\vec{e}^1_1 = \vec{e}^{1*}_2\,;\ \vec{e}^1_3 = \vec{e}^{1*}_6\,;\ \vec{e}^1_4 = \vec{e}^{1*}_5\,.$$

Combining this new information with the form of $\underline{e}^1$ from Eq. (A7) we obtain

$$\underline{e}^1 = (a00; a^*00; g0k; g\,0\,-k; g^*0\,-k; g^*0k^*)\,. \qquad \text{(A9)}$$

Expressing the eigenvector components in terms of an amplitude and phase

$$e^j_{\kappa\alpha} = \epsilon^j_{\kappa\alpha} e^{i\phi^j_{\kappa\alpha}}\,,$$

we can interpret the above form of $\underline{e}^1$ in terms of sets of equations relating the $\epsilon^j_{\kappa\alpha}$ and $\phi^j_{\kappa\alpha}$:

$$\begin{aligned}
&\epsilon^1_{1x} = \epsilon^1_{2x}\,, \quad \phi^1_{1x} = -\phi^1_{2x}\,,\\
&\epsilon^1_{3x} = \epsilon^1_{4x} = \epsilon^1_{5x} = \epsilon^1_{6x}\,, \quad \phi^1_{3x} = \phi^1_{4x} = -\phi^1_{5x} = -\phi^1_{6x}\,,\\
&\epsilon^1_{3z} = -\epsilon^1_{4z} = -\epsilon^1_{5z} = \epsilon^1_{6z}\,, \quad \phi^1_{3z} = \phi^1_{4z} = -\phi^1_{5z} = -\phi^1_{6z}\,,
\end{aligned} \qquad \text{(A10)}$$

all others being zero. We now see explicitly the six independent quantities which are needed to specify an eigenvector of Σ_1 symmetry. The atomic displacement pattern characteristic of this eigenvector is shown in Fig. 7. The form of the eigenvectors for the other three representations have been worked out as well, and they are summarized in Table V.

*Present Address: Bell Laboratories, Murray Hill, New Jersey, 07974. Worked based in part on the thesis by D. E. Moncton, submitted in partial fulfillment of the requirements for the Ph.D. degree to Massachusetts Institute of Technology, 1975.

†Work performed under the auspices of the U. S. ERDA.

[1]J. A. Wilson and A. D. Yoffe, Adv. Phys. 18, 193 (1969).

[2]J. A. Wilson, F. J. DiSalvo, and S. Mahajan, Phys. Rev. Lett. 32, 882 (1974); Adv. Phys. 24, 117 (1975).

[3]D. E. Moncton, J. D. Axe, and F. J. DiSalvo, Phys. Rev. Lett. 34, 734 (1975).

[4]T. M. Rice and G. K. Scott, Phys. Rev. Lett. 35, 120 (1975).

[5]S.-K. Chan and V. Heine, J. Phys. F 3, 795 (1973).

[6]This sample was a "batch D" crystal of Ref. 7.

[7]D. J. Huntley and R. F. Frindt, Can. J. Phys. 52, 861 (1974).

[8]Recent experiments measuring the Young's modulus of $TaSe_2$ have shown a sharp anomaly near 90 K which exhibits a 5 °K hysteresis. See M. Barmatz, in *Proceedings of the Ultrasonics Symposium, Milwaukee, Wisconsin*, 1974 (IEEE, New York, 1974).

[9]A. Arrott and S. A. Werner, Phys. Rev. Lett. 14, 1022 (1965).

[10]L. J. Vieland, R. W. Cohen, and W. Rewald, Phys. Rev. Lett. 26, 373 (1971).

[11]See, however, A. W. Overhauser, Phys. Rev. 133, 3173 (1971).

[12]John A. Holy, Miles V. Klein, W. L. McMillan, S. F. Meyer, Phys. Rev. Lett. 37, 1145 (1976).

[13]An additional displacement wave can arise from higher-order coupling terms in the free energy.

[14]R. M. Nicklow, N. Wakabayashi, and H. G. Smith, Phys. Rev. B 5, 4951 (1972).

[15]N. Wakabayashi, H. G. Smith, and R. M. Nicklow, Phys. Rev. B 12, 659 (1975).

[16]N. Wakabayashi, H. G. Smith, and H. R. Shanks, Phys. Lett. A 50, 367 (1974).

[17]N. Wakabayashi (private communication).

[18]R. J. Birgeneau, J. Skalyo, and G. Shirane, Phys. Rev. B 3, 1736 (1971).

[19]L. D. Landau and E. M. Lifshitz, *Statistical Physics* (Addison-Wesley, Reading, Mass., 1958), Chap. XIV.

[20]W. L. McMillan, Phys. Rev. B 12, 1187 (1975).
[21]P. C. Kwok and P. B. Miller, Phys. Rev. 151, 387 (1966).
[22]W. L. McMillan, Phys. Rev. B 14, 1496 (1976).
[23]A. A. Maradudin and S. H. Vosko, Rev. Mod. Phys. 40, 1 (1968).
[24]A. A. Maradudin, E. W. Montroll, and G. H. Weiss in *Solid State Physics*, edited by F. Seitz and D. Turnbull (Academic, New York, 1965), Suppl. 3.
[25]O. V. Kovalev, *Irreducible Representation of the Space Groups* (Academy of Sciences of the Ukranian SSR, Kiev, 1961) [English translation: (Gordon and Breach, New York, 1964).]
[26]M. Tinkham, *Group Theory and Quantum Mechanics* (McGraw-Hill, New York, 1964).
[27]This equation is a simplified form of Eq. (4.12), Ref. 23.